Int J Biometeorol
DOI 10.1007/s00484-014-0844-2

ORIGINAL RESEARCH PAPER

Footprint methods to separate N_2O emission rates from adjacent paddock areas

Sandipan Mukherjee · Andrew M. S. McMillan · Andrew P. Sturman · Mike J. Harvey · Johannes Laubach

Received: 19 July 2013 / Revised: 1 May 2014 / Accepted: 2 May 2014

Abstract Using micrometeorological techniques to measure greenhouse gas emissions from differently treated adjacent plots is a promising avenue to verify the effect of mitigation strategies at the field scale. In pursuing such an approach, it is crucial to accurately characterize the source area of the fluxes measured at each sampling point. Hence, a comprehensive footprint analysis method is required so that emission rates can be obtained for a specific field within a biochemically heterogeneous area. In this study, a footprint analysis method is developed to estimate the emission for an experiment where the flux of N_2O is measured from several control and treated plots. The emission rate of an individual plot is estimated using an inverse footprint fraction approach where the footprint fractions are obtained from an analytical footprint model. A numerical solution for obtaining the background flux for such a multiplot measurement system is also provided. Results of the footprint analysis method are assessed, first, by comparing footprint fractions obtained from both an analytical footprint model and a "forward" simulation of a backward Lagrangian stochastic (bLs) model; and second, by comparing the emission rates of a control plot obtained from the footprint analysis method and from the "backward" simulation of the bLs model. It is found that the analytical footprint fractions compare well with the values obtained from the bLs model (correlation coefficient of 0.58 and 0.66 within p value <0.001). An average of 4.3 % of the measured fluxes is found to be contributed by sources outside the measured area and, excluding this outside area contribution to the measured flux, footprint corrected emission rates within the defined domain are found to increase by 2.1 to 5.8 % of the measured flux. Also, the proposed method of emission rate estimation is found to work well under a wide range of atmospheric stability.

Keywords N_2O emission · Footprint method · Kormann and Meixner model · Backward Lagrangian model

S. Mukherjee (✉) · A. P. Sturman
Centre for Atmospheric Research, University of Canterbury, Christchurch, New Zealand
e-mail: sandipanmukherjee@hotmail.com

A. M. S. McMillan
Landcare Research, Private Bag 11052, Palmerston North 7640, New Zealand

M. J. Harvey
National Institute for Water and Atmospheric Research, 301 Evans Bay Parade, Wellington, New Zealand

J. Laubach
Manaki Whenua–Landcare Research, Gerald St, Lincoln 7608, New Zealand

Present Address:
S. Mukherjee
G.B. Pant Institute of Himalayan Environment and Development, Kosi-Katarmal, Almora 263643, India

Abbreviations

Abbreviations of some repeatedly used terms with their units in parentheses:

C_b	Background concentration (ppb)
F_0	Background flux ($gN_2O\text{-}N\ ha^{-1}\ day^{-1}$)
bLs model	Backward Lagrangian stochastic model
ΔC	Concentration gradient (ppb)
EC	Eddy covariance
$ER_{F^0_{eqn}}$	Emission rate from the analytical solution of F_0 ($gN_2O\text{-}N\ ha^{-1}\ day^{-1}$)
FG	Flux gradient
f_p	Footprint function
γ	Footprint fraction
$\gamma_{outside}$	Footprint fraction from outside source area
$u_\star$	Friction velocity ($m\ s^{-1}$)
f_p^{max}	Maximum of footprint function
U_{mean}	Mean wind speed ($m\ s^{-1}$)

Published online: 05 June 2014

L	Obukhov length (m)
PSA	Principal source area
z_0	Roughness length (m)
σ_v	Standard deviation of lateral wind component (m s^{-1})

Introduction

Increasingly, there is a need to understand how agricultural trace gas emissions are affected by management practices, particularly those directed at greenhouse gas emissions mitigation (Soussana et al. 2007; Leytem et al. 2011). For nitrous oxide (N_2O), the most potent greenhouse gas released from agricultural operations, the great majority of experiments have used the static chamber method (De Klein et al. 2013). With this method, individual measurements are made at the scale of an experimental plot (~1 m^2), usually with a number of replicates and often to compare the effects of two or more treatments to each other. While these studies have been invaluable in testing the efficacy of treatments at these small scales, there remains considerable uncertainty in upscaling to the field because of the following known limitations with the static chamber technique (Denmead 2008): (1) the limited spatial coverage of even a large number of replicates does not allow representative sampling of the spatial variability of a field, (2) typical sampling frequency is insufficient to capture the temporal dynamics of fluxes, and (3) the closure of chambers interferes with the natural processes of gas exchange between a vegetated surface and the atmosphere.

Micrometeorological techniques are ideally suited for quantifying trace gas exchange at the agricultural field scale (Harper et al. 2011; Denmead 2008): the spatial scale of measurement (>1 ha) is similar to an operational unit of management, say a dairy paddock or a crop field; they integrate across spatial heterogeneity that occurs at smaller spatial scales and they measure continuously, capturing the often episodic nature of fluxes. However, in contrast to static chambers, the spatial domain (or footprint) of micrometeorological techniques is not known a priori due to variations in local meteorological conditions. Generally, a retrospective analysis known as "flux footprinting" is required to determine the source area of a particular flux measurement (Schmid 1994). Flux footprinting becomes particularly crucial when a micrometeorological technique is deployed in a comparative mode, which necessarily involves multiple adjacent field plots (Neftel et al. 2008). The experimenter will need to quantify the portion of a measured flux that originated from within the plot of interest, and therefore assess the flux contribution from areas outside the target and/or from other treatment plots. This paper is a methodological paper aimed at addressing this need.

The design of a multiple-plot micrometeorological experiment will involve several gas sampling points, each positioned to measure fluxes predominantly from one of several adjacent upwind target field plots (Pattey et al. 2006). Ideally, each sampling point will be sampling fluxes only from its associated upwind field plot. Inevitably, on some occasions, contamination from adjacent areas will occur. Footprint models for the atmospheric surface layer have matured to an extent that the amount of contamination from adjacent field plots can be quantified with confidence (Neftel et al. 2008). Furthermore, since both fluxes and footprint fractions are calculated at each sampling point over a common time interval, fluxes from the same field-scale plot are measured by two or more sampling locations. This creates an opportunity to estimate emissions from each field-scale plot when the flux footprint extends beyond the target plot using a sufficiently determined set of linear equations. Such an approach was first attempted by Van de Boer et al. (2013), for sensible heat fluxes.

Here, a numerical method is developed to estimate trace gas emissions from a set of adjacent plots using this inverse footprint approach. The method is tested on a real-world experimental data set in which the efficacy of a N_2O mitigation strategy was tested in a multiple-plot micrometeorological experiment (McMillan et al. 2014). A validation of the footprint fractions is carried out using footprint fractions obtained from a "forward" simulation of the backward-Lagrangian stochastic model (bLS) of Flesch et al. (1995). Furthermore, emission rates obtained from the proposed linear-algebra method are compared with emission rates obtained from the same bLs model executed in normal mode (i.e., computing backwards from measured concentration data as inputs). The approach outlined here provides a means to (1) quantify the extent of flux contamination from nontarget areas, and (2) calculate emission rates from field plots during periods when contamination is substantial.

Experimental setup and measurements

The N_2O data of the field experiments described in McMillan et al. (2014) are used in this study where the N_2O fluxes were measured from an agricultural paddock in Canterbury, New Zealand, in separate experiments conducted in autumn and spring, 2010. The measurement campaign in autumn was carried out from 9 May 2010 to 21 June 2010, and in spring from 24 September 2010 to 22 November 2010. Figure 1 shows the location of subplots and instrument towers in a Cartesian coordinate system. The experimental paddock was aligned approximately 340° to true north. The field is mapped to a coordinate system relative to an origin (0, 0), which is the location of the primary sonic anemometer, referred to as the Gill (model: WindMaster Pro, Gill Instruments, Lymington, UK), shown as EC-2 in Fig. 1. A secondary sonic anemometer (model: CSAT3, Campbell Scientific Inc., UT, USA) is shown

as EC-1 in Fig. 1. Both sonic anemometers were installed at 2-m height. Atmospheric vertical profiles were measured at location G-1, and thermocouples and cup anemometers were mounted on a meteorological mast. Temperature sensors or free-spanned resistance wires (diameter <20 μm) were installed at 2.49, 1.30, and 0.55 m, and cup anemometers were installed at 2.72, 1.52, 0.72, and 0.40 m. This experimental set up was maintained in both campaigns. The flux gradient (FG) gas inlets are shown as G-1 to G-4 in the diagram. Operation of these inlets was similar to that mentioned in Wagner Riddle et al. (2007). Air samples were collected at each of these masts using a lower gas inlet at 0.5 m and a higher gas inlet at 1.0 m. A tunable diode laser (model: TGA100A, Campbell Scientific, Logan, Utah) was used to measure the N_2O concentrations differences. The measurement field was divided into three control subplots (A, C, and E of Fig. 1) and two experimental subplots (B and D of Fig. 1) with an approximate width of 140 m and length of 100 m each. Fluxes were measured in a switching cycle such that for one averaging period (30 min in autumn, 20 min in spring), air was sampled only from one mast, alternating rapidly (every 9 s in autumn and 6 s in spring) between the two intake heights. For the subsequent averaging periods, air from each of the masts was sampled in a sequence (i.e., air from mast G-1 to G-4 was sampled in a switching cycle). Details of the gas sampling and raw N_2O data processing can be found in McMillan et al. (2014). The shorter integrating time was used in the spring experiment to obtain a greater number of samples of the N_2O flux.

During the filtering procedure, only those data were accepted where (i) $-0.5 \leq 1/L \leq 0.5$, where L is the Obukhov length (m), (ii) $u_\star > 0.075$ m s^{-1}, where $u_\star$ is the friction velocity (m s^{-1}), and (iii) $u_\star/U_{mean} < 0.2$, where U_{mean} is the mean wind speed at the measurement height (m s^{-1}). The turbulent eddy diffusivities were estimated using a parameterized approach and subsequently nitrous oxide fluxes were computed. Details of these computations including estimation of L and $u_\star$ values are provided in Mukherjee et al. (2014). Both Gill and CSAT3 sonic anemometer measurements were used for flux footprint analysis and footprint fraction estimation.

Field treatment Since the purpose of the research reported here is to provide a footprint analysis method for an experiment where fluxes of N_2O are measured from several control and treated plots, a detailed description of field management of the experimental paddock is provided here. However, a comparative analysis of the magnitude of N_2O fluxes between two treatments is not the aim of this study. The experimental paddock (blue rectangle of Fig. 1) including subplots A–E were treated with different chemicals at different times, and these treatments were documented with date and time. Surrounding paddocks of the experimental field were occasionally grazed and were not chemically treated. The N_2O mitigation experiments were carried out using the nitrification inhibitor DCD with different concentrations of urea and cow-urine only for subplots B and D. Therefore, subplots A, C, and E are termed "control plots" and subplots B and D are termed "mitigated plots." The soil type of the field site was Lismore silt loam. Details of the Lismore silt loam soil type in the Canterbury region of New Zealand can be found in Di and Cameron (2002). The entire paddock was grazed by 450 cows twice during the autumn experiment and by 428 cows three times during the spring experiment. Details of the field activity, including dates of grazing and chemical applications over the experimental site, are provided in Table 1.

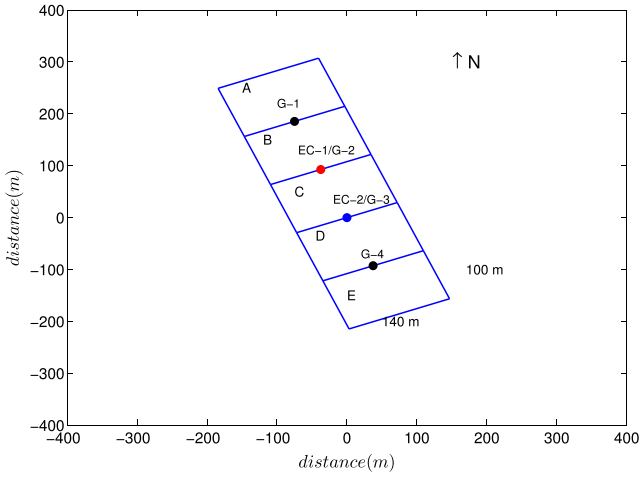

Fig. 1 Layout of the measurement field showing subplots *A–E*. The control plots are *A*, *C*, and *E* and the mitigated plots are *B* and *D*. EC-1 is the location of the CSAT3 anemometer, EC-2 is the location of the Gill anemometer, G-1 to G-4 are the FG gas intake positions

Methods

Details of the numerical approach of emission rate from multiplot flux measurement are described in the "Numerical setup for estimating emission rate" section. This new approach largely depends on the "footprint fraction" of each field, where footprint fraction denotes the percentage contribution of each field to the total measured flux at each mast as obtained from a standard footprint model. In this study, the footprint fractions are obtained from the footprint model of Kormann and Meixner (2001) using the code of Neftel et al. (2008). A brief description of the model including its implementation is described in "Analytical flux footprint model" section. Finally, a backward Lagrangian stochastic model (bLs) is used for comparison of results which is described in "Backward Lagrangian model" section.

Table 1 Description of the field activity

Season	Date	Activity
Autumn	09-May-10	Measurement began
	11 to 13 May-10	Grazing - 1 entire paddock
	14-May-10	65 kg/ha ammonium urea fertilizer applied over the entire paddock
	19-May-10	DCD applied to plot B and plot D
	30-May to 2-June-10	Grazing - 2 entire paddock
	21-Jun-10	Measurement finished
Spring	24-Sep-10	Measurement began
	28–29 Sep-10	Grazing - 1 entire paddock
	07-Oct-10	DCD applied to plot B
	12-Oct-10	30 kg/ha liquid urea applied to whole paddock extra 30 kg/ha urea applied to plot D
	20-22 Oct-10	Grazing - 2 entire paddock
	06-08 nov-10	Grazing - 3 entire paddock
	22-Nov-10	Measurement finished

Numerical setup for estimating emission rate

The goal of this work is to compute the emission rates from the rectangular plots A to E based on N_2O flux measurements at the locations shown in Fig. 1. The solutions for northerly wind directions are described in the following, but they are also valid for southerly winds if indices A to E and 1 to 4 are reversed. Here, the "northerly" and "southerly" wind bisector terminologies are used as generic terminologies, i.e., for a field with 0° alignment with true north, northerly wind would represent a regime of 270-0-90° (clockwise). However, depending on the alignment of the field, the degree of bisectors has to be adjusted. We can denote the emission rates by ER_A, …, ER_E and with a matrix notation ER. Vertical fluxes were measured at four masts on the boundaries between these plots and denoted by F_1, ..., F_4. Now, if only the northerly wind bisector is considered, fluxes (F_1, ..., F_4 having matrix notation F) will not only depend on the corresponding emission rates from rectangles A to D, but will also depend on the emission rate north of subplot A, denoted as ER_N. We assume ER_N to be spatially uniform with infinite extent in the upwind direction. Given this definition of ER_N, it must be equal to the flux F_0 that would have been measured at the upwind boundary of subplot A, had there been a measurement mast. We can then write the emission rates and the fluxes as a five-component vector. These vectors are related by a 5×5 matrix, the footprint fraction matrix (Γ), with elements γ_{ij} obtained from any analytical footprint model as follows:

$$\begin{pmatrix} F_0 \\ F_1 \\ F_2 \\ F_3 \\ F_4 \end{pmatrix} = \begin{pmatrix} \gamma_{0N} & \gamma_{0A} & \gamma_{0B} & \gamma_{0C} & \gamma_{0D} \\ \gamma_{1N} & \gamma_{1A} & \gamma_{1B} & \gamma_{1C} & \gamma_{1D} \\ \gamma_{2N} & \gamma_{2A} & \gamma_{2B} & \gamma_{2C} & \gamma_{2D} \\ \gamma_{3N} & \gamma_{3A} & \gamma_{3B} & \gamma_{3C} & \gamma_{3D} \\ \gamma_{4N} & \gamma_{4A} & \gamma_{4B} & \gamma_{4C} & \gamma_{4D} \end{pmatrix} \begin{pmatrix} ER_N \\ ER_A \\ ER_B \\ ER_C \\ ER_D \end{pmatrix} \quad (1)$$

Here, γ_{ij} is the footprint fraction obtained from mast i for plot j. The above equation can be represented by a more compact notation as follows:

$$F_i = \sum_j \Gamma_{ij} ER_j \quad (2)$$

where i=0, .. , 4 and j=N, A, B, C, D. Now in Eq. 1, symbols γ_{1N} to γ_{4N} can be calculated as the outside flux contribution at each mast and γ_{0A} to γ_{0D} as equal to 0. The footprint analysis procedure is restricted to subplots A to D as subplot E is a terminal control plot having a similar effect to subplot A. Note that $0 \le \gamma_{ij} \le 1$ for each row of the matrix and the elements must add up to 1. We further note that the diagonal elements will usually be the largest elements of a given row, reflecting the dominant influence of the nearest plot on a flux measurement. For a northerly wind, the elements to the right of the diagonal will be 0 because the plots downwind of a mast have no influence on their flux observations. Furthermore, for a 340° wind, aligned with the field orientations, conditions (i) $\gamma_{2A}=\gamma_{3B}=\gamma_{4C}>0$, (ii) $\gamma_{3B}>\gamma_{3A}>0$, and (iii) $\gamma_{4C}>\gamma_{4B}>\gamma_{4A}>0$ are satisfied.

Emission rates can be obtained by inverting Eq. 2 as follows:

$$ER_j = \sum_i H_{ji} F_i \quad (3)$$

where $H_{ji}=(\Gamma_{ij})^{-1}$ and Eq. 3 can be expressed as

$$\begin{pmatrix} ER_N \\ ER_A \\ ER_B \\ ER_C \\ ER_D \end{pmatrix} = \begin{pmatrix} \eta_{N0} & \eta_{N1} & \eta_{N2} & \eta_{N3} & \eta_{N4} \\ \eta_{A0} & \eta_{A1} & \eta_{A2} & \eta_{A3} & \eta_{A4} \\ \eta_{B0} & \eta_{B1} & \eta_{B2} & \eta_{B3} & \eta_{B4} \\ \eta_{C0} & \eta_{C1} & \eta_{C2} & \eta_{C3} & \eta_{C4} \\ \eta_{D0} & \eta_{D1} & \eta_{D2} & \eta_{D3} & \eta_{D4} \end{pmatrix} \begin{pmatrix} F_0 \\ F_1 \\ F_2 \\ F_3 \\ F_4 \end{pmatrix} \quad (4)$$

Here, $\eta_{..}$ are the elements of the vector H. The matrix inversions were carried out using the inverse command of the MATLAB software. Now, condition $H_{ji} \subset \Re$, where $\Re$ is a real number series, will only be satisfied if the diagonal elements of $\gamma_{ij} \neq 0$; although, the cases that were observed

where diagonal elements of γ_{ij} were missing for both autumn and spring experiments when no EC measurements were available. It is to be noted that the γ values were obtained from the footprint analysis tool of Neftel et al. (2008, described below) using the 30-min EC measurements. Therefore, γ values were not available for those cases where EC measurements were not available. Such cases where three or more diagonal elements of γ_{ij} were missing were completely ignored; although for cases where two or more diagonal elements of γ_{ij} were missing, a maximum possible weight of 0.97 was assumed. The 97 % footprint fraction value was found to be the most probable value for our experimental setup under a steady wind and neutral conditions.

The first row of Eq. 4 collapses to $F_0=ER_N$, but this term is unknown and will be solved below. The emission rates of different plots can be estimated directly from Eq. 4. Here, we focus on plot A and C as they are control plots that can be used to estimate F_0. To estimate ER_A, flux measurements made at mast G-1 and G-2 were considered. However, to estimate ER_C, flux measurements made at masts G-1 to G-4 were used. Therefore, ER_A and ER_C are represented as follows:

$$ER_A = F_0\eta_{A0} + F_1\eta_{A1} + F_2\eta_{A2} \tag{5}$$

and

$$ER_C = F_0\eta_{C0} + F_1\eta_{C1} + F_2\eta_{C2} + F_3\eta_{C3} + F_4\eta_{C4} \tag{6}$$

Equations 5 and 6 can be used to estimate the emission rates from subplots A and C if instantaneous flux values are available for F_1,..,F_4 and the F_0 value is known. Since at an instantaneous time all the four fluxes (F_1,..,F_4) were not available from our measurements, synchronized time series of flux values were prepared for each mast using a linear temporal interpolation.

In the case of estimating unknown F_0, an algebraic relationship can be obtained for F_0 by assuming $ER_A=ER_C$, as both plots received similar management, as follows:

$$F_0 = \frac{\eta_{C1}-\eta_{A1}}{\eta_{A0}-\eta_{C0}}F_1 + \frac{\eta_{C2}-\eta_{A2}}{\eta_{A0}-\eta_{C0}}F_2 + \frac{\eta_{C3}}{\eta_{A0}-\eta_{C0}}F_3 + \frac{\eta_{C4}}{\eta_{A0}-\eta_{C0}}F_4 \tag{7}$$

In theory, the solution of Eq. 7 is unique and exact. In practice, we have to be very cautious because of the numerical uncertainty of the measured fluxes, and also because some elements of the η_{ji} matrix are not very different from 0. These are the two components of Eq. 7 which can make the numerical solution of F_0 unstable. Inserting realistic example values, one can see that F_0 is obtained as a small difference of the two almost equally strongly weighted flux terms F_1 and F_3 with a minor correction from F_2 and F_4, with much lower weights. Therefore, any measurement error or discontinuity in the difference of F_1 and F_3 will cause a huge error in F_0.

The numerical constraints for this method, including the solution of Eq. 7, have already been described above. For further application of F_0 to compute ER_A and ER_C, only those cases should be used to compute F_0 where the flux footprint is relatively large and therefore the nondiagonal elements of the γ-matrix are substantial and $|F_1-F_3|$ is minimal. Again, one has to note that each F_0 value computed following this approach cannot be directly fed back to Eqs. 5 and 6 for individual emission rate estimation as algebraic equality between ER_A and ER_C has been assumed. Therefore, a statistically significant and physically meaningful value of F_0 obtained from Eq. 7 should be used. The procedure for F_0 estimation is described below and emission rates estimated using the F_0 value are represented by $ER_{F_{eqn}^0}$.

Now, if the assumption of equality of emission rates from control plots holds true throughout the experimental period, irrespective of time, then F_0 computed by the above method can be used to compute emission rates from the mitigated plots (e.g., plots B and D). Therefore, emission rate equations can be derived for subplots B and D similar to Eqs. 5 and 6. Hence, this approach can be applied to any other measurement setup where equality of the emission rates can be assumed for heterogeneous plots when deriving the unknown background flux.

Analytical flux footprint model

The analytical flux footprint model of Kormann and Meixner (2001) is a suitable model for scalar flux footprint estimation from an eddy covariance (EC) measurement system. The model uses the solution of an advection diffusion equation for a power law profile of mean wind velocity and diffusivity. The two-dimensional footprint function for a fixed measurement height obtained from this model is expressed as follows (Kormann and Meixner 2001):

$$f_p(x,y) = \frac{1}{\sqrt{2\pi}Dx^E} exp\left(-\frac{y^2}{2Dx^E}\right) Cx^{-A} exp\left(-\frac{B}{x}\right) \tag{8}$$

Where the A, B, C, D, and E terms are discussed in detail in Kormann and Meixner (2001) and Neftel et al. (2008). A visual basic application-based program of this model was developed by Neftel et al. (2008), which also included coordinates of the measurement field and instrument locations. The model approximates the footprint function contours and

footprint fraction of individual fields based on the EC measurements of $u_\star$, wind direction, L, standard deviation of the lateral wind component (σ_v), and horizontal wind speed (assumed to be equal to U_{mean}).

This analytical footprint model was used in the current footprint analysis. The measurement height (z_m) was assumed to be the geometric mean height of the gas inlets, equal to 0.86 m, above a displacement height d=0.066 m. Ideally, meteorological instruments should be located exactly at the same height as the flux gradient inlets, but because of the noncollocation of these instruments, averages of the gas inlet measuring heights with wind profile instrument heights were used. Therefore, z_1=0.478 m and z_2=1.41 m were used in $z_m=\Delta z_{2-1}/\ln(z_2/z_1)$ (Laubach and Kelliher 2004) to estimate measurement height. The emission rates were estimated based on the footprint information of this analytical model and compared with the backward Lagrangian stochastic model output.

The time averaged (30- and 20-min values of autumn and spring) values of $u_\star$, wind direction, L, σ_v, and U_{mean} were fed into the analytical footprint model along with the field coordinates and z_m. The model output consisted of (i) z_0, (ii) footprint function (f_p), (iii) footprint fraction from each subplots (γ), which is a fraction of the total integral of footprint function for a particular domain and estimated based on the predefined coordinates of the domain, and (iv) values of the constants A–E and distances for calculating the semi-major and semi-minor axes of the footprint area, which is assumed to be an ellipse. The ellipses mark the boundary of the emitting surface area, where the footprint function drops to 1 % of its maximum value. It should also be noted that the footprint function is asymmetric in nature and therefore, source areas close to the measurement mast will have higher contribution to the measured flux (Neftel et al. 2008). The peak location of the footprint function, f_p^{max}, was estimated by calculating the distance (R) from the measurement tower to the centre of the ellipse using output of the code provided by Neftel et al. (2008; see the manual for the code at http://www.agroscope.admin.ch/art-footprint-tool/). Finally, the Cartesian coordinate of the centre of the ellipse (x_0, y_0) was estimated following Eq. 9.

$$\left.\begin{aligned} x_0 &= R\cos\theta_{rad} + x_{mast} \\ y_0 &= R\sin\theta_{rad} + y_{mast} \end{aligned}\right\} \tag{9}$$

Where θ_{rad} is the wind direction in radians and x_{mast} and y_{mast} are the x and y coordinates of the mast. However, it is important to note that the elliptical shape of the footprint area can change with stability and wind speed. Therefore, the f_p^{max} values computed from the above method may not be necessarily the actual representation of f_p^{max}, but a close approximation. The footprint analysis of our sonic anemometer data was performed based on the dominant surface wind regimes as described in "Footprint from analytical models."

Backward Lagrangian model

The bLs model used for this study was *WindTrax* version 2.0.8.4. This model is based on Flesch et al. (1995) and has been widely used for paddock scale flux footprint estimation (Laubach and Kelliher 2005; Flesch et al. 2005; Bjorneberg et al. 2009; Laubach 2010). Since the bLs model is used in this study only for testing the numerical footprint approach, no detailed model description is provided here, but can be found in Flesch et al. (1995, 2004, 2005). However, it is to be noted that the bLs model derives air parcel trajectory touchdown statistics in a flow field that is horizontally homogeneous and where the wind profile is logarithmic with standard Monin-Obukhov stability corrections. The touchdown statistics provide a direct link between the emission rate of a confined area and the concentration differences between the locations upwind and downwind of this area. The particular model setup for our field experiment is described below.

bLs model setup

The WindTrax model was setup only for subplot A, as this plot was a control and terminal plot and required only a single continuous simulation for emission rate estimation. The measurement plot was defined by a rectangle of width 140 m and length 100 m. The field orientation was 340° with respect to true north. A fixed z_0 of 0.03 m, following Laubach (2010), was used in all the simulations considering z_0 as 1/10 of grass height. Instead of using the sonic anemometer turbulent intensity measurements directly in the WindTrax setup, prefiltered time-averaged wind speed, wind direction, and temperature were provided directly to the model. Similarly, L measurements were used directly in the WindTrax surface layer model.

Since the proposed approach to estimation of emission rate largely depends on the footprint fraction values obtained from the Kormann and Meixner (2001) model, at first, (i) the analytical footprint fractions were compared with values obtained from a "forward" simulation of the bLs setup. "Forward" shall mean here that the emission rate is prescribed and the resulting concentration gradients downwind are computed; note that the air parcel trajectories are still modeled backwards in time. This is distinct from a true forward simulation, where the air parcels are tracked forward in time from their origin. Such a forward-in-time simulation is computationally efficient only for problems with a small number of discrete point sources. This would also verify the consistency of the analytical footprint model of Kormann and Meixner (2001) under different atmospheric stability

conditions and confirm that the module is realistic. Next, (ii) the source area emission rates of the control plots obtained from the proposed numerical setup (Eqs. 5 and 6) of "Numerical setup for estimating emission rate" section ($ER_{F^0_{eqn}}$) were compared with the emission rates obtained from the "backward" simulations of the bLs model (ER_{model}). Since a proper background concentration (abbreviated as C_b) was not measured during both of our field experiments, and the bLs predicted emission rates (ER_{model}) can vary substantially depending on the background concentrations of N_2O (Flesch et al. 2004), the ER_{model} values were estimated by using concentration measurements at the 0.5 and 1-m height of each mast for a single source area. The measurement masts were fixed upwind to the plots and no C_b values were prescribed, instead the C_b values were obtained as model output. This WindTrax setup is overdetermined in theory, but limited in practice by (i) the proximity of the paired concentration measurements to each other (optimizing for WindTrax would mean placing air intakes into quite separate locations; by contrast, our priority was to place intakes close enough to each other that a meaningful turbulent diffusivity could be used to get a local vertical flux), and (ii) by measurement resolution issues in general. The bLs model setup for the "forward" and "backward" simulations is described as follows:

The bLs model setup for forward simulation The bLs model for this case was simulated in a "forward mode" to estimate footprint fractions (γ) from the concentration gradients elevated above the background. The WindTrax model was simulated only for subplot A, defined as the emitting area, of the autumn and spring experiments. Similar to Fig. 1, all the rectangular subplots were described in the model along with four measurement masts having concentration sensors at 0.5 and 1.0 m. The measured concentrations were defined as unknown at each mast and the C_b values were fixed to 0 for subplot A. The measured emission rates for subplot A were defined as equal to 1. The observed wind and turbulence data were provided to the "surface layer model" and to the "atmosphere model" of WindTrax. The forward simulation of this setup would then produce the elevated concentrations at 0.5 and 1.0-m height at each mast and the concentration gradients (ΔC) can be estimated for each mast. As a result, the footprint fractions of subplot A can be estimated from the bLs model at each mast following:

$$\gamma_{A_1(bLs)} = \Delta C_1/(\Delta C_1 + \Delta C_2 + \Delta C_3 + \Delta C_4 + \Delta C_0) \quad (10)$$

where $\gamma_{A_1(bLs)}$ is the footprint fraction measured at G-1 for subplot A from the bLs model and ΔC_0 is the extra gradient term unaccounted for by the masts. Similarly, $\gamma_{A_{2,\ldots,4}}(bLs)$ can be estimated. Now, it has to be kept in mind that Eq. 10 and the abovementioned condition would be satisfied if the wind direction is aligned with the field, when the ΔC_0 term should approach 0. Therefore, for simplicity, only those cases were considered below where the wind direction was between 320 and 360° to represent an approximate northerly aligned wind (a total of 186 and 296 values for autumn and spring, respectively). Results of these forward simulations are described in "Comparison with analytical model."

The bLs model setup for backward simulation Emission rates from each control plot were obtained using a similar set up described above, except for the fact that both 0.5 and 1-m concentrations were used as known concentrations and no C_b values were provided. Rather, C_b was produced as model output from the "backward" run of the model. Since measured concentrations were provided at two heights with unknown emission rates from a single plot, a unique solution for this setup was available. Results of these backward simulations are described in "Comparison with analytical model."

A total of 20,000 particles were released for each simulation and case, and the particle dispersion track was followed up to 600 and 300 m, respectively, for the "forward" and "backward" simulation experiments. This particle track distance covers the entire field in all directions.

Results and discussion

Footprint from analytical models

The footprint analysis of each measurement mast was carried out based on the prevailing surface wind directions of both field campaigns. These were found to be north-northeasterly (NNE), north-northwesterly (NNW), and southwesterly (SW) for both autumn and spring experiments. The wind distributions for both of our experiments are shown in Fig. 2. During the autumn experiment, three predominant wind regimes were observed: 0–50° (NNE) with 18.1 % of the total data and an average wind speed of 2.60 m s^{-1}; 300–360° (NNW) with 33.9 % of the total data with an average wind speed of 1.94 m s^{-1}; and 200–260° (SW) with 22.0 % of the total data with an average wind speed of 2.63 m s^{-1}.

Wind regimes for the spring experimental period are shown in Fig. 2b. The dominant wind direction in spring was NNE (0–100°) with 45.3 % of the total observations and an average wind speed of 2.11 m s^{-1}. NNW winds (300–360°) constituted 24.1 % of the total observations with an average wind speed of 3.12 m s^{-1}, and SW winds (200–260°) represented only 9.3 % of the total observations with an average wind speed of 2.69 m s^{-1}.

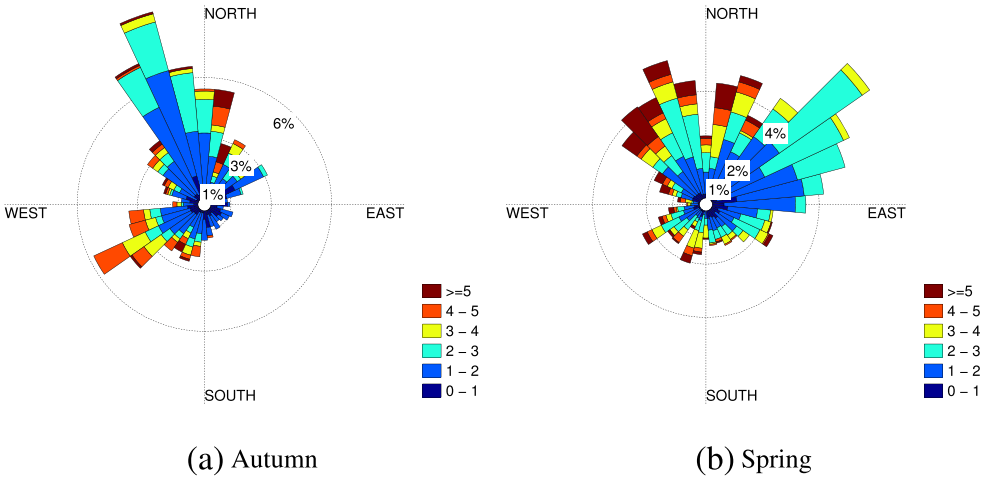

Fig. 2 Wind distribution for **a** the autumn campaign and **b** for the spring campaign. Wind sectors are subdivided based on wind speed (m s^{-1})

Footprint for the EC-1/G-2 mast Coordinates of the f_p^{max} under NNE winds are shown in Fig. 3a (left panel) for autumn and 3a (right panel) for spring as an example. Each f_p^{max} coordinate in the diagram is, therefore, a function of instantaneous wind direction. Similarly, Fig. 3b (upper panel) and 3b (lower panel) show the maximum footprint fractions (γ) for the same wind regimes and for the autumn and spring campaigns. The principal source areas (PSA) of the measured fluxes, where γ is maximum, along with the mean values of the peak distances of footprint functions, $\overline{f_p^{max}} = 1/N\sum_N^1 f_p^{max}$, at EC-1/G-2 for all the three subplots are shown in Table 2 for both seasons. The height-to-fetch ratios for all the stability classes were found to be within 1:100. From the f_p^{max} and $\overline{f_p^{max}}$ values, it was evident that, predominantly, most of the fluxes measured at EC-1/G-2 location were coming from within the boundaries of the subplots. The atmospheric stability conditions were mostly neutral, 40.2 and 56.9 % of the time for NNE, and 59.4 and 46.3 % for NNW, respectively, for the

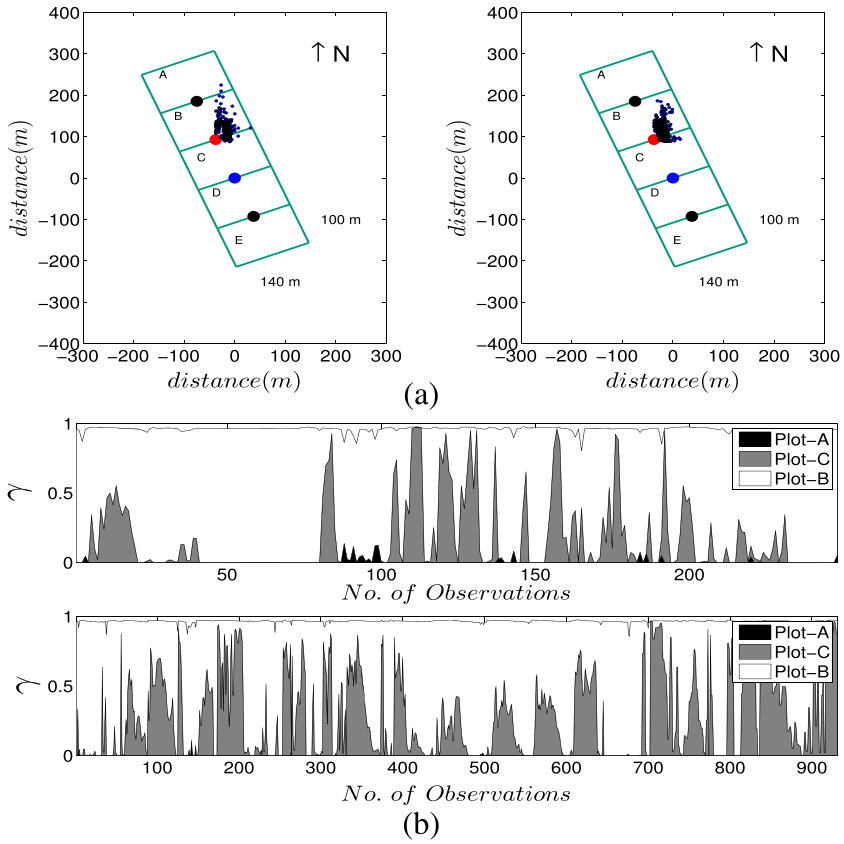

Fig. 3 **a** The locations of 30/20 min f_p^{max} from the measurement mast for only the NNE wind regime (*left panel* for autumn and *right panel* for spring). Location of the EC-1/G-2 mast is represented with the *red circles* in between subplots *B* and *C*. **b** The maximum footprint fraction (γ) values for subplots for only the NNE wind regime at the EC-1/G-2 mast. *Upper panel* is for autumn and *lower panel* is for the spring campaign

Table 2 Percentage contributions of the principal source areas (PSA) to fluxes measured at the EC-1/G-2 location for different wind regimes

Wind regime	Source area information for EC-1			
	autumn		spring	
	PSA(%)	$\overline{f_p^{max}}$(m)	PSA(%)	$\overline{f_p^{max}}$(m)
NNE	Subplot B (79.6 %)	38.7	Subplot B (68.0 %)	29.7
NNW	Subplot B (90.9 %)	59.4	Subplot B (95.2 %)	41.0
SW	Subplot C (70.4 %)	44.6	Subplot C (70.2 %)	41.3

Mean values of peak distance of the footprint function, $\overline{f_p^{max}}$, are also shown

autumn and spring experiments. Similar results were obtained for the EC-2/G-3 mast where the principal source area contributing the measured flux was found to be subplot C for NNE and NNW wind regime and subplot D for SW wind regime, respectively.

Footprint for the G-1/G-4 mast We have already mentioned that the sonic anemometers were placed at locations EC-1 and EC-2, and no sonic anemometer measurements were available for the G-1 and G-4 locations, but to get an idea of the source area contribution to the measured flux values at G-1 and G-4, the CSAT3 measurements were used at these locations by assuming that the surface layer turbulence is homogeneous over flat terrain. Similar to the EC-1/2 analysis, γ values from individual subplots were also estimated for G-1 and G-4, and the results were used to estimate the source area emission rate of individual subplots.

Source area outside the measurement paddock It is evident from Fig. 3b that $(\sum_{i=1}^{5} \gamma_i) \neq 1$, where i represents the number of subplots. This implies that a source area outside the predefined area of interest also contributed to the flux measurement at the individual measurement locations. Therefore, the footprint fraction outside our area of interest ($\gamma_{outside}$) was computed following $\gamma_{outside} = 1 - \sum_{i=1}^{5} \gamma_i$. Variations in the $\gamma_{outside}$ values as a function of wind direction and surface layer stability are shown in Fig. 4. Both EC-1 and EC-2 data were used to produce this diagram. The maximum contribution of source area outside all of our experimental subplots was found to be of the order of 30 %, irrespective of the measurement masts and plots (Fig. 4b).

One can see from Fig. 4 that except for some occasional high values of $\gamma_{outside}$, contributions from outside the source area remained minimal. The mean $\gamma_{outside}$ value, irrespective of measurement mast and experimental campaign, was found to be 0.043 (4.3 %), which is significantly lower than the contribution from the principal source areas. High values of $\gamma_{outside}$ were mostly found to be associated with higher atmospheric surface layer stability ($1/L > 0.1$). Again, when the effect of geometry of the plot relative to $\gamma_{outside}$ was considered for a stable atmosphere, most of the high values were observed when the wind was diagonal to the field, and particularity high $\gamma_{outside}$ values were observed when the wind direction was between 225 and 255°.

Measured fluxes and emission rates from control plots A and C

Flux values were measured at individual masts, where each mast was located at the interface of two subplots. Now, these measured flux values from each mast can be assigned to each plot depending on northerly or southerly wind bisectors if no footprint correction is assumed. For example, the flux measured at the G-1 mast location in Fig. 1 can be assigned to plot A for a northerly wind bisector and plot B for a southerly wind, respectively. Such assignment of measured flux to a specific subplot based on wind directions is a good approximation of actual emission rate if the footprint ellipse covers the described source area. Such values are termed as "measured flux ($Flux_p$)" in this section and computed for each subplot. Measured flux values as well as standard errors (SE) in the measurements of subplots A and C for both autumn and spring experiments are shown in Table 3. Cases were only chosen for comparison where both measured fluxes and emission rates were available (e.g., $Flux_p$ and $ER_{F_{eqn}^0}$). The SE values were calculated following $SE = \sigma_{var}/\sqrt{n}$, where σ_{var} was the standard deviation of *var* (*var* is $Flux_p$ and *ER*) and n is the number of data. $Flux_P$ of Table 3 represents the measured flux obtained using the parameterized transfer coefficients.

When F_0 was estimated using Eq. 7, some unrealistically large negative/positive values were observed ($|F_0| > 1{,}000$ $gN_2O\text{-}N\ ha^{-1}\ day^{-1}$). As mentioned in "Numerical setup for estimating emission rate," these cases were detected when differences between F_1 and F_3 were high ($|F_1 - F_3| > 5$ $gN_2O\text{-}N\ ha^{-1}\ day^{-1}$) and contributions from term 2 and/or 4 of the right-hand side of Eq. 7 were significant. All such high values were discarded and only those F_0 values were accepted where the numerical solution of Eq. 7 had physical meaning. Although such observations were few, lower and upper limits

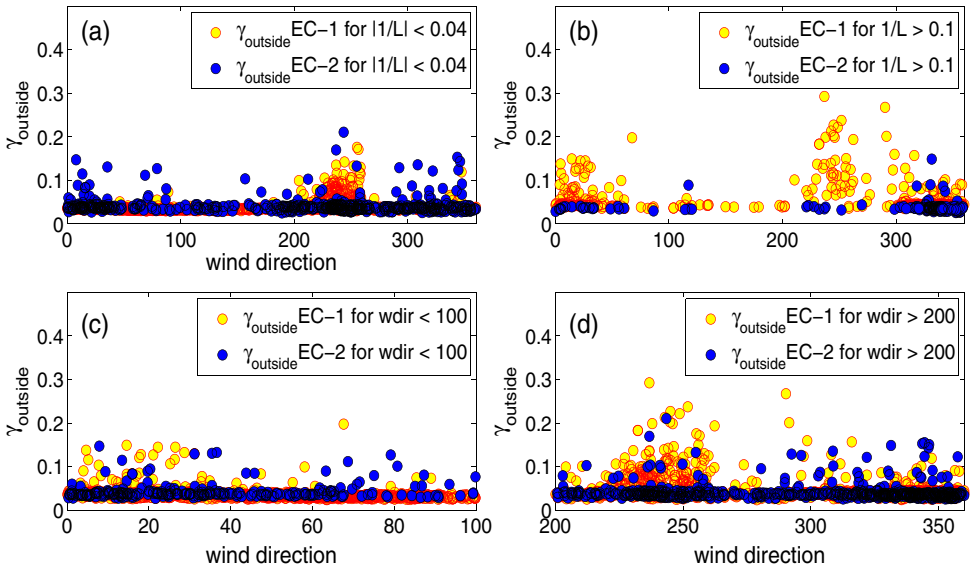

Fig. 4 The $\gamma_{outside}$ values of both autumn and spring are plotted for **a** a neutral atmosphere ($|1/L|<0.04$) and **b** a stable atmosphere ($1/L>0.1$) using measurements at masts EC-1 and EC-2. Similarly, outside values of both autumn and spring are plotted for **c** NNE and **d** NNW and SW wind regimes irrespective of stability and using measurements at masts EC-1 and EC-2

of such values were found to be between $0 \leq F_0 \leq 15.0$ gN_2O-N ha^{-1} day^{-1}. However, a mean value of $F_0=6.77$ gN_2O-N ha^{-1} day^{-1} was used in Eqs. 5 and 6 to estimate emission rates for both seasons. The emission rates, obtained using F_0 in Eq. 7 are shown in Table 3. Emission rate estimates were found to be higher than the $Flux_p$ values. The maximum variation between $Flux_p$ and $ER_{F^0_{eqn}}$ estimates was 0.5 gN_2O-N ha^{-1} day^{-1} for the control plots, irrespective of season, which was on average 2.1 % higher than the measured flux. However, depending on the variation of F_0, $ER_{F^0_{eqn}}$ values were found to increase up to 6 %. A higher actual emission rate than the measured flux is expected under an approximately fixed background flux of N_2O as the footprint fraction will seldom have the idealistic value of 1 and corresponding η value. This will signify a fractional mapping between the measured flux and emission rate.

To explore the effect of stability on the ER_A and ER_C values obtained from the numerical method, $ER_{F^0_{eqn}}$ and $Flux_p$ are plotted as functions of $1/L$ in Fig. 5 for both autumn (Fig. 5a, b) and spring campaigns (Fig. 5c, d). Most of the fluxes and emission rates were obtained while $-0.3 \leq 1/L \leq 0.3$ and comparatively high values were observed when $1/L \geq 0$. Since the proposed method performs a flux partitioning within several multiplots, the correlation coefficients between fluxes and emission rates were always high (>0.90).

Table 3 Arithmetic mean ± standard error of the selected measured flux and emission rate of N_2O in gN_2O-N ha^{-1} day^{-1} for the autumn and spring experiments are denoted by "arithmetic"

Seasons	N_2O flux gN_2O-N ha^{-1} day^{-1}		
	Plots	$Flux_p$	$ER_{F^0_{eqn}}$
Autumn	$A_{arithmetic}$	9.4±1.28 (100)	9.4±1.34 (100)
	$B_{arithmetic}$	11.4±1.44 (122)	11.8±1.53 (122)
	$C_{arithmetic}$	14.1±2.74 (98)	14.6±2.84 (98)
	$D_{arithmetic}$	11.6±2.94 (97)	11.9±3.06 (97)
Spring	$A_{arithmetic}$	13.1±2.16 (229)	13.6±2.20 (229)
	$B_{arithmetic}$	12.3±0.93 (278)	13.2±1.02 (278)
	$C_{arithmetic}$	12.5±1.61 (230)	12.8±1.54 (230)
	$D_{arithmetic}$	12.1±1.26 (215)	13.4±1.42 (215)

Emission rates are estimated using F_0 from Eq. 7 ($ER_{F^0_{eqn}}$). Observations were only used for this comparison where both measured flux and emission rate values were available. The total number of such observations is shown in parenthesis. A and C represent the control and B and D represents the treated subplots of the experimental paddock

Emission rates from the treated plots B and D

Similar to subplots A and C, source area emission rates are estimated for subplots B and D in this section. The F_0 values used for this computation were obtained from Eq. 7. It has to be kept in mind that a similar mitigation treatment can have different results for two different plots, and examining the effect of mitigating efforts on N_2O flux in an open environment is a completely different study as the controlling factors of mitigation can be many. Therefore, no in-depth analysis of the effect of mitigation on N_2O flux values has been performed here and only some initial results are provided.

Similar to subplots A and C, when the $Flux_p$ values were compared with the $ER_{F^0_{eqn}}$ values, the maximum variation was found to be 1.2 gN_2O-N ha^{-1} day^{-1} for plot D of the spring experiment (9.9 % enhancement). Again, $ER_{F^0_{eqn}}$ values were found to be on average 5.8 % higher than $Flux_p$ for subplots B and D, respectively (Table 3). No significant reduction in the emission rate between DCD treated and control plots were observed. Previously, it was also mentioned that subplot D

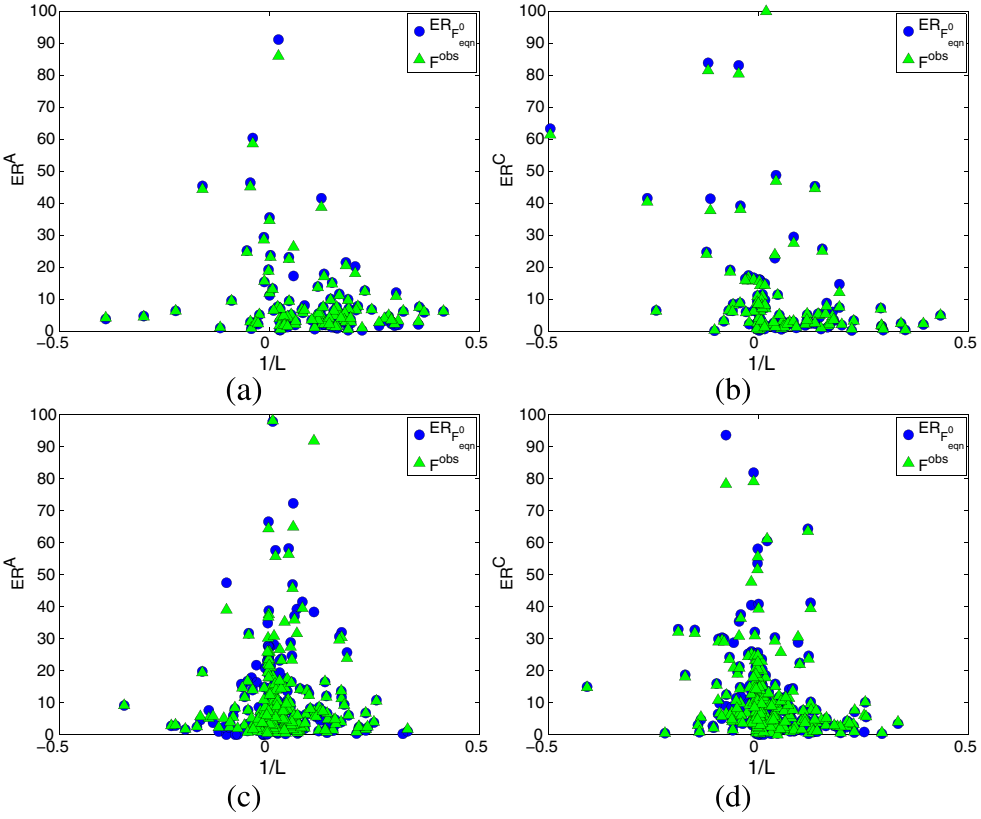

Fig. 5 Selected emission rates ($ER_{A,C}$) and observed flux values (F_{obs}) in $gN_2O\text{-}N\ ha^{-1}\ day^{-1}$ are represented as functions of inverse Obukhov lengths (1/L) in m^{-1} for (**a**, **b**) autumn and (**c**, **d**) spring campaigns of subplots *A* and *C*, respectively

was treated with extra ammonia during spring, but no enhancement in the $Flux_p$ values was observed from this analysis, although a 0.1 $gN_2O\text{-}N\ ha^{-1}\ day^{-1}$ enhancement was observed in the $ER_{F^0_{eqn}}$ values when compared with values from plots A, B, and C. However, it is to be noted that this comparison was made based on the selected data samples only and the effect of mitigation on N_2O emission rate might change with a larger dataset.

Comparison with analytical model

Footprint fraction values from forward simulation of the bLs model When the γ_{A_1} values were compared with the $\gamma_{1_A}(bLs)$ values from forward simulation of the bLs model, a systematic bias was observed in $\gamma_{1_A}(bLs)$ values. This systematic bias is intrinsic to our WindTrax setup as the emission rate of outside source area was not accounted for with any flux measurement mast. To compensate for this error, $\gamma_{1_A}(bLs)$ values were further computed using $\Delta C_0 = 0.1\Delta C_1$. This 10 % estimate was obtained after a small sensitivity study. The new ΔC_0 values were then used to estimate $\gamma_{1_A}(bLs)$ values. Ratios of the γ_{A_1} and $\gamma_{A_1}(bLs)$ as a function of $1/L$ are shown in Fig. 6a. The mean absolute differences in footprint fraction values ($|E| = |\overline{\gamma_{A_1}} - \overline{\gamma_{A_1}(bLs)}|$) are shown in the lower panels of the same figure. For the autumn experiment, marginally higher $|E|$ values were observed for $1/L > 0$ cases with an overall high observed correlation coefficient (0.58 with p value <0.001) between $\gamma_{A_1}(bLs)$ and γ_{A_1}, whereas a correlation coefficient value of 0.66, with p value <0.001, was observed in spring between $\gamma_{A_1}(bLs)$ and γ_{A_1}. On average, a 10 % enhancement in these correlation coefficient values was observed when only the near-neutral ($|1/L| < 0.1$) cases were considered.

Surface emission rates from the backward simulation of the bLs model Emission rates obtained using the backward simulation of the bLs model are shown in Fig. 7 for the autumn and spring experiments, respectively. During the comparison, 10 and 30 of the ER_{bLs} values of autumn and spring were neglected as they were unrealistically large ($ER_{bLs} >$ 1,500 $gN_2O\text{-}N\ ha^{-1}\ day^{-1}$). These values were mostly associated with $1/L \geq 2.0$ and/or high wind speed (ws) ≥4.0 m s^{-1}. The correlation coefficients between $ER_{F^0_{eqn}}$ and ER_{bLs} for both seasons were found to be 0.70 and 0.61, respectively, with p value <0.0005. Similarly, the slopes of the regression lines were found to be 0.91 and 0.43, respectively, for autumn and spring.

Error analysis of the analytical footprint model

Uncertainty in the analytical footprint model is quantified in this section. Instead of deriving an algebraic equation for the relative error in the footprint function, a sensitivity analysis has been performed using the footprint tool developed by

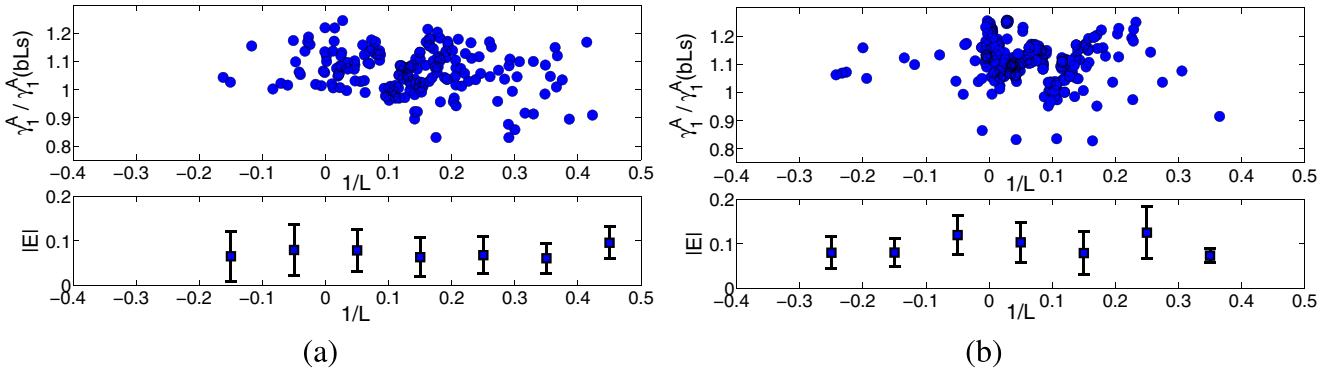

Fig. 6 Ratios of the footprint fraction values obtained from the analytical footprint model and the bLs model ($\gamma_{1A}/\gamma_{1A}(bLS)$) for subplot A represented versus 1/L of the **a** autumn and **b** spring experiment. The observed mean and standard deviation of errors ($|E|$) between the two footprint fractions are shown in the bottom panels for respective seasons

Neftel et al. (2008). The previous study by Neftel et al. (2008) has shown that the longitudinal variation of the footprint function largely depends on the $U_{mean}/u_\star$ ratio, which reflects the strength of horizontal advection with respect to vertical diffusion. Neftel et al. (2008) has also correlated the z_0 values with the $U_{mean}/u_\star$ ratios and found an approximate 25 % change in the footprint values when z_0 was changed by a factor of 2, but the effect of stability was ignored as most of the analyzed cases were for a near neutral surface layer. Instantaneous z_0 values were computed for both G-2 and G-3 masts and compared with observations. The model-simulated mean z_0 values for the southwesterly and north-northwesterly wind regimes of our experiment were found to be approximately ±1.5 times lower/higher than the observed value, resulting in an approximately 18.75 % change in f_p, whereas the model-simulated mean z_0 value for the north-northeasterly wind regime was found to be approximately equal to the observed value except for very few high cases (a total of four observations were higher). Therefore, the average relative error in f_p due to variation in z_0 ($R_{z_0}^{f_p}$) would be of the order of 0.125 (12.5 %).

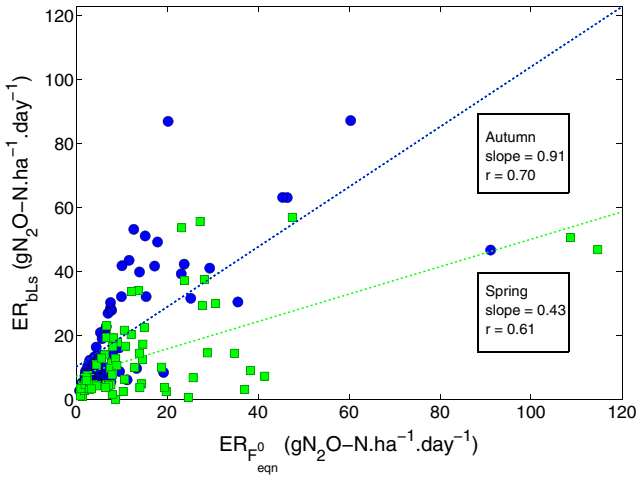

Fig. 7 Comparison of emission rates from the numerical method ($ER_{Fo_{eqn}}$) and bLs model (ER_{bLS}) for subplot *A* of autumn (shown in *blue circles*) and spring (shown in *green squares*) campaigns. The *blue* and *green lines* indicate the fitted linear regression between $ER_{Fo_{eqn}}$ and ER_{bLs}. The intercept and correlation coefficient (r) values for each campaign are shown inside the *textboxes*

Furthermore, changes in f_p were estimated by changing the input variables L, σ_v, $u_\star$, and U_{mean} of the model within a reasonable range for $1/L>0$ and for $1/L\leq 0$ cases. The surface source area of our model was already defined, so that the sensitivity of f_p was tested over a domain of 100×140 m for a north-northeasterly wind (wind direction=42.24° and z_m= 0.86 m) and for a fixed set of data σ_v=0.18, $u_\star$=0.15 m s^{-1} and U_{mean}=1.38 m s^{-1}.

For a stable atmospheric case of $1/L$=0.1, if the $1/L$ values were perturbed within a range of ±50.0 %, the mean change in the f_p value was found to be between 1.3 and 2.6 %, indicating the mean relative error in f_p from variations in $1/L$ ($R_{1/L}^{f_p}(s)$) is of the order of 0.0195 (1.95 %). The 50 % error range was chosen for the L term because $u_\star$ and heat flux terms contribute substantially to L as they can have errors between 10 and 15 %. Similarly, when $1/L$ was assumed to be −0.1 (unstable), the mean relative error in f_p from $1/L$ ($R_{1/L}^{f_p}(u)$) was found to be of the order of 0.0172 (1.72 %). "*s*" and "*u*" indicate stable and unstable atmospheres.

Next, the $u_\star$ values were also perturbed with a ±10.0 % error for stable ($1/L$=0.1) and unstable ($1/L$=−0.1) cases. The $R_{u_\star}^{f_p}(s)$ was found to be 0.0068 (0.68 %) and the $R_{u_\star}^{f_p}(u)$ was found to be 0.0017 (0.17 %). Similarly, for U_{mean}, $R_{U_{mean}}^{f_p}(s)$ was found to be 0.00625 (0.625 %) and $R_{U_{mean}}^{f_p}(u)$ was found to be 0.0017 (0.17 %); and for σ_v, $R_{\sigma_v}{}^{f_p}(s)$ was found to be 0.0005 (0.05 %) and $R_{\sigma_v}{}^{f_p}(u)$ was found to be 0.0001 (0.01 %). Compared to the relative error from z_0 ($R_{z_0}^{f_p}$), errors from L, σ_v, $u_\star$, and U_{mean} were found to be very small, although it should be noted that the error sensitivity analysis was performed only for a ±10.0 % error range and only mean values were considered, rather than maximum values. Finally, the mean random error in f_p was estimated as follows:

$$R^{f_p} = \left(R_{z_0}^{f_p}{}^2 + R_{1/L}^{f_p}{}^2 + R_{u_\star}^{f_p}{}^2 + R_{U_{mean}}^{f_p}{}^2 + R_{\sigma_v}^{f_p}{}^2 \right)^{1/2} \qquad (11)$$

The $R^{f_p}(s)$ value was found to be in the order of 0.1288 (12.88 %), whereas the $R^{f_p}(u)$ value was found to be 0.1266 (12.66 %). Now, if we consider that the total uncertainty in our emission rate values is the summation of error from the diffusivity parameter ($R_{d_h^p}$), concentration gradients ($R_{\Delta C_{N_2O}}$) and footprint function (R^{f_p}), then the mean propagated error in the emission rates (R_{flux}^{Mean}), $R_{flux}^{Mean} = \sqrt{R^{p2} + R^{f_p 2}}$, would be approximately of the order of 16.53 % irrespective of stability, where R_p is described in McMillan et al. (2014) and Mukherjee et al. (2014). R_p for stable and unstable atmospheric conditions was found to be 0.12 (12 %) and 0.09 (9 %), respectively, with a mean value of 0.105 (10.5 %) when averaged over all stability classes.

Conclusion

A method has been developed to account for varying footprint functions in a multiplot micrometeorological comparison of N_2O fluxes. Such multiplot measurement systems are becoming common, and examples includes Wagner Riddle et al. (2007). The framework incorporated a calculation of footprint fractions using the model of Kormann and Meixner (2001), together with solving a set of linear equations to estimate source area emission rate for a specific field treatment. A mathematical solution of background flux has been provided for those situations where no background flux measurement was made. Since this new approach of emission rate estimation is fundamentally dependent on the footprint fraction values of a particular multiplot field experiment, footprint fractions obtained from the analytical footprint model were tested with values from a bLs model. The analysis revealed that 4.3 % of the fluxes attributed to treatment plots (without footprint correction) were contaminated with fluxes from outside the plot boundaries. The maximum amount of contamination was 30 %. The background flux when computed using the numerical solution provided in this study was found to be sensitive to the measured flux and atmospheric surface layer flow properties. However, the proposed emission rate estimation formulae have been found to work well. The actual emission rates from the proposed method were found to be on average 2.1 and 5.8 % higher than the measured flux values for the control and mitigated plots, respectively. These enhancements in the emission rate values are due to the footprint correction which includes the surface layer flow properties and the geometry of the field. A higher actual emission rate than the measured flux is expected under an approximately fixed background flux of N_2O, as the footprint fraction will seldom have the idealistic value of 1 and corresponding flux value.

To verify the consistency of the analytical footprint model for varying atmospheric stabilities, a forward simulation of a backward Lagrangian stochastic model was used to derive footprint fractions which were compared. A good agreement (correlation coefficients of 0.58 and 0.66) between the analytical and the bLs model footprint affirms the realistic nature of the analytical model. The correlation coefficients were found to increase by 10 % when only the near neutral cases were considered. Finally, when the emission rates obtained from this new approach were compared with the bLs simulated emission rates of a control plot, it was found that the proposed method worked well when the atmospheric stability $|1/L| \leq 0.2$.

This study has focused on the development of a method of estimation of surface emission rates from the measured flux and footprint fractions, which also includes the field geometry and atmospheric surface layer flow. Therefore, an in-depth analysis of the effect of mitigation on the treated plot was not performed. Although our initial comparison between the control and treated plot showed no significant difference in the emission rates, effects of mitigation may be observed if this procedure is applied to a larger data or for a different experiment. Since the overall footprint corrected emission rate values were not significantly different from the measured flux values assigned to each plot based on the wind bisectors, readers might ask why such a detailed footprint correction is of interest. The answer to this question lies in the fact that geometry and location of sensors plays a very important role in a multiplot measurement setup as "Unfortunately, emission rate estimates for multisource problems are often badly behaved, with spurious predictions obtained comparably often to appropriate values (Raupach 1989)"; (quoted from (Crenna et al. 2008), pp. 7373). Therefore, a rigorous footprint analysis is necessary for multiplot flux measurement, irrespective of the end product. Again, it has to be remembered that rigorous data processing is necessary before one uses this approach for actual source area emission rate estimation. Extra precautions should be taken for computing the background flux following our proposed mathematical formula as it is highly sensitive to the input measured flux values.

Acknowledgments This project was funded by the Sustainable Land Management and Adaptation to Climate Change Fund of the Ministry for Agriculture and Forestry (now Ministry for Primary Industries) contract CO1X0816, by New Zealand's Foundation of Research, Science and Technology (FRST) until 2011.

References

Bjorneberg D, Leytem A, Westermann D, Griffiths P, Shao L, Pollard M (2009) Measurement of atmospheric ammonia, methane and nitrous oxide at a concentrated dairy production facility in southern Idaho using open-path FTIR spectrometry. Trans Am Soc Agric Biol Eng 52(5):1749–1756

Crenna BP, Flesch TK, Wilson JD (2008) Influence of source-sensor geometry on multi-source emission rate estimates. Atmos Environ 42(32):7373–7383

De Klein C, Harvey M, Alfaro M, Chadwick D, Clough T, Grace P, Kelliher F, Rochette P, Venterea R (2013) A common protocol for measuring N_2O fluxes using chamber methods. Adv Anim Biosci 4: 223

Denmead O (2008) Approaches to measuring fluxes of methane and nitrous oxide between landscapes and the atmosphere. Plant Soil 309(1):5–24. doi:10.1007/s11104-008-9599-z

Di H, Cameron K (2002) The use of a nitrification inhibitor, dicyandiamide DCD, to decrease nitrate leaching and nitrous oxide emissions in a simulated grazed and irrigated grassland. Soil Use Manag 18:395–403. doi:10.1079/SUM2002151

Flesch T, Yee E, Wilson J (1995) Backward-time Lagrangian stochastic dispersion models and their application to estimate gaseous emissions. J Appl Meteorol Climatol 34(6):1320–1332. doi:10.1175/1520-0450(1995)034<1320:BTLSDM>2.0.CO;2

Flesch T, Wilson J, Harper L, Crenna B, Sharpe R (2004) Deducing ground-to-air emissions from observed trace gas concentrations: a field trial. J Appl Meteorol 43:487–502

Flesch T, Wilson J, Harper L, Crenna B (2005) Estimating gas emissions from a farm with an inverse-dispersion technique. Atmos Environ 39:4863–4874. doi:10.1016/j.atmosenv.2005.04.032

Harper L, Denmead O, Flesch T (2011) Micrometeorological techniques for measurement of enteric greenhouse gas emissions. Anim Feed Sci Technol 166–167:227–239

Kormann R, Meixner F (2001) An analytical footprint model for non-neutral stratification. Bound-Layer Meteorol 99(2):207–224

Laubach J (2010) Testing of a Lagrangian model of dispersion in the surface layer with cattle methane emissions. Agric For Meteorol 150(11):1428–1442. doi:10.1016/j.agrformet.2010.07.006

Laubach J, Kelliher F (2004) Measuring methane emission rates of a dairy cow herd by two micrometeorological techniques. Agric For Meteorol 125(3–4):279–303. doi:10.1016/j.agrformet.2004.04.003

Laubach J, Kelliher F (2005) Measuring methane emission rates of a dairy cow herd (ii): results from a backward-Lagrangian stochastic model. Agric For Meteorol 129(3–4):137–150. doi:10.1016/j.agrformet.2004.12.005

Leytem A, Dungan R, Bjorneberg D, Koehn A (2011) Emissions of ammonia, methane, carbon dioxide, and nitrous oxide from dairy cattle housing and manure management systems. J Environ Qual 40: 1383–1394

McMillan A, Harvey M, Ross M, Bromley A, Evans M, Mukherjee S, Laubach J (2014) The detectability of nitrous oxide mitigation efficacy in intensively grazed pastures using a multiple plot micrometeorological technique. Atmos Meas Tech 7:1169–1184. doi:10.5194/amt-7-1169-2014

Mukherjee S, Sturman A, McMillan A, Harvey M, Zawar-Reza P (2014) Assessment of error propagation in measured flux values of an eddy diffusivity based micrometeorological setup. Atmos Environ 84: 144–155. doi:10.1016/j.atmosenv.2013.10.034

Neftel A, Spirig C, Ammann C (2008) Application and test of a simple tool for operational footprint evaluations. Environ Pollut 152(3): 644–652. doi:10.1016/j.envpol.2007.06.062

Pattey E, Edwards G, Strachan I, Desjardins R, Kaharabata S, Wagner Riddle C (2006) Towards standards for measuring greenhouse gas fluxes from agricultural fields using instrumented towers. Can J Soil Sci 86:373–400

Raupach MR (1989) Applying Lagrangian fluid mechanics to infer scalar source distributions from concentration profiles in plant canopies. Agric For Meteorol 47(2):85–108

Schmid H (1994) Source areas for scalars and scalar fluxes. Bound-Layer Meteorol 67(3):293–318

Soussana JF, Fuhrer J, Jones M, Van Amstel A (2007) The greenhouse gas balance of grasslands in Europe. Agric Ecosyst Environ 121(1): 1–4. doi:10.1016/j.agee.2006.12.001

Van de Boer A, Moene A, Schüttemeyer D, Graf A (2013) Sensitivity and uncertainty of analytical footprint models according to a combined natural tracer and ensemble approach. Agric For Meteorol 169:1–11

Wagner Riddle C, Furon A, McLaughlin NL, Lee I, Barbeau J, Jayasundara S, Parkin G, Von Bertoldi P, Warland J (2007) Intensive measurement of nitrous oxide emissions from a corn-soybean-wheat rotation under two contrasting management systems over 5 years. Glob Chang Biol 13(8):1722–1736